Supporting information

Unraveling the relationship between phenethylammonium-induced 2D phase on the perovskite surface and inverted wide bandgap perovskite solar cell performance

Xiaomin Huo [1,2], Silvia Mariotti [1], Yaoyao Li [2], Ting Guo [1], Chenfeng Ding [1], Penghui Ji [1], Shuai Yuan [1], Tongtong Li [1], Ning Meng [2], Xiaomin Liu [1], Jiahao Zhang [1], Ilhem Nadia Rabehi [1], Yu Zhang [2], Suling Zhao [2], Hengyuan Wang [1], Dandan Song [2], Luis K. Ono [*1], Zheng Xu [*2], Yabing Qi [*3]

[1] Energy Materials and Surface Sciences Unit (EMSSU), Okinawa Institute of Science and Technology Graduate University (OIST), 1919-1 Tancha, Onna-son, Kunigami-gun, Okinawa 904-0495, Japan

[2] Key Laboratory of Luminescence and Optical Information, Beijing Jiaotong University, Ministry of Education, Beijing 100044, China.

[3] Global Institute of Future Technology, Shanghai Jiao Tong University, Shanghai 200240, P. R. China.

* Corresponding authors: Luis K. Ono, E-mail: katsuya.ono@oist.jp; Zheng Xu, E-mail: zhengxu@bjtu.edu.cn; Yabing Qi, E-mail: yabingqi@sjtu.edu.cn

Table of contents

Experimental Section

Materials

The [4-(3,6dimethyl-9H-carbazol-9-yl)butyl]phosphonic acid (Me-4PACz), 1,6-hexylenediphosphonic acid (6dPA), lead iodide (PbI_2, 99.99%), lead bromide ($PbBr_2$, >98.0%) phenethylammonium chloride (PEACl), phenethylammonium bromide (PEABr), phenethylammonium iodide (PEAI), and bathocuproine (BCP) were purchased from Tokyo Chemical Industry Co. (TCI), Japan. Formamidinium iodide (FAI), methylammonium bromide (MABr, >98.0%) were purchased from the Dyenamo. Cesium iodide (CsI) was purchased from Sigma-Aldrich. [6,6]-phenyl C61 butyric acid methyl ester ($PC_{61}BM$) was purchased from Advanced Election Technology Co., Ltd (China). The solvents, including ethanol (super dehydrated, 99.5%), N,N-dimethylformamide (DMF), dimethyl sulfoxide (DMSO), ethyl acetate (EA), and isopropanol (IPA) were purchased from Wako Pure Chemical Co., Ltd. The 1,2-dichlorobenzene (ODCB, 98+%, Extra Dry, AcroSeal) was purchased from ACROS.

Device Fabrication

ITO glass substrates were cleaned with detergent, deionized water, acetone, and isopropanol under ultrasonication for 30 min, respectively. The substrates were dried by N_2 flow and then treated with UV - ozone for 15 min. The Me-4PACz solution was prepared with the mixture of Me-4PACz (1 mg/ml in ethanol) and 6dPA (1 mg/ml in ethanol) in 85:15 v:v ratio. The solution was sonicated for 10 minutes and then spin-coated at 3000 rpm for 30 s in the fume hood, after which the substrates were annealed at 100 ℃ for 5 minutes. Then the substrates were transferred to the N_2-filled glovebox. The perovskite ($Cs_{0.05}(FA_{0.77}MA_{0.23})_{0.95}Pb(I_{0.77}Br_{0.23})_3$) precursor solution was prepared by dissolving PbI_2 (583.71mg), $PbBr_2$ (138.43 mg), FAI (201.19 mg), MABr (39.12 mg), and CsI (20.78 mg) in 800 μl DMF and 200 μl DMSO. The perovskite precursor was stirred on a stirring hotplate at 60 ℃ for around 1.5 hours before use. After the precursor solution cooled down, it was filtered with a 0.45 μm PTFE filter, and then

spin-coated on the Me-4PACz/ITO substrates at 5000 rpm for 90 s with 200 µl ethyl acetate dripping at 40 s during the spin-coating process, and finally annealed at 100 ℃ for 30 minutes. The $Cs_{0.2}FA_{0.8}Pb(I_{0.8}Br_{0.2})_3$ perovskite precursor solution was prepared by dissolving PbI_2 (461.01mg), $PbBr_2$ (91.75 mg), FAI (128.98 mg), FABr (31.24 mg), and CsI (64.95 mg) in 624 µl DMF and 208 µl DMSO. The $MAPbI_3$ perovskite precursor solution was prepared by dissolving PbI_2 (931.2 mg), MAI (318 mg) in 1060 µl DMF and 146 µl DMSO. The perovskite precursor was stirred on a stirring hotplate at 60 ℃ for around 1.5 hours before use. After the precursor solution cooled down, it was filtered with a 0.45 µm PTFE filter. The $Cs_{0.2}FA_{0.8}Pb(I_{0.8}Br_{0.2})_3$ precursor solution was spin-coated on the Me-4PACz/ITO substrates at 5000 rpm for 90 s with 200 µl ethyl acetate dripping at 40 s during the spin-coating process, and finally annealed at 100 ℃ for 30 minutes. The $MAPbI_3$ precursor solution was spin-coated on the Me-4PACz/ITO substrates at 3000 rpm for 40 s with 200 µl ethyl acetate dripping at 15 s during the spin-coating process, and finally annealed at 100 ℃ for 20 minutes. When the PEAX solution was used, a solution in IPA (with different concentration depending on the PEAX used and the perovskite composition) was prepared and spin-coated directly on the perovskite layer at 4000 rpm for 30 s without any other treatment. Then, if annealing was performed, this was performed at 100 ℃ for 10 min. Afterward, $PC_{61}BM$ (20 mg/ml in ODCB) solution, filtered with 0.22 µm PVDF filter, was spin-coated onto the perovskite layer at 1000 rpm for 45 s and then annealed at 70 ℃ for 10 minutes. The BCP (2 mg/ml in IPA) solution, was sonicated for 10 minutes and then filtered with 0.22 µm PVDF filter, and then spin-coated onto the $PC_{61}BM$ layer at 6000 rpm for 30 s and then annealed at 70 ℃ for 5 minutes. Finally, the 80 nm silver electrode were evaporated onto the substrate under high vacuum (< 10^{-7} Torr) to fabricate solar cell devices. The active area of the devices is 0.16 cm^2.

Characterization

The X-ray diffraction (XRD) data were collected by a Bruker D8 Discover diffractometer (Bruker AXS) using a Cu (λ = 1.54 Å) X-ray source with the power of

1600 W. The grazing-incidence wide-angle X-ray scattering (GIWAXS) data were obtained at 1W1A Diffuse X-ray Scattering Station, Beijing Synchrotron Radiation Facility (BSRF-1W1A). Scanning electron microscopy (SEM) was conducted by Microscopy FEI Quanta 250 FEG to obtain the surface morphology of the perovskite films. X-ray photoelectron spectroscopy (XPS) and angle-depended XPS analysis were carried out on KRATOS AXIS ULTRA DLD equipped with monochromatic Al Kα (1486.6 eV). The time-of-flight secondary ion mass spectrometry (ToF-SIMS) measurements were performed on the Model ToF-SIMS 5 (ION-ToF GmbH) instrument with the pulsed primary ions from a $GCIB^+$ (10 keV) ion gun for the sputtering and a Bi_1^+ pulsed primary ion beam for the analysis (30 keV). The SIMS setup (Kratos Axis ULTRA) is equipped with an Ar^+ sputtering gun (1 keV, 50 nA beam current and 100 um spot size) and a quadrupole mass spectrometer (HAL 7, Hiden Analytical) operated in the positive ion detection mode. The SIMS is performed at a pressure of 10^{-8} Torr.[1] The ultraviolet photoemission spectra (UPS) (He-Iα = 21.22 eV) were collected by a photoelectron spectrometer (XPSAXIS Ultra HAS, Kratos). Low-energy inverse photoemission spectroscopy (LEIPS, ALS Technology Co., Ltd) measurements were performed in a high-vacuum chamber with a pressure of 10^{-10} Torr. Time-resolved photoluminescence (TRPL) was carried out with the FLS1000 instrument using a 450 nm picosecond pulsed laser. The current-voltage (*J-V*) curves of the device were recorded by a Keithley 2400 Source Meter under simulated solar illumination AM 1.5G (100 mW cm^{-2}). The EQE spectra of devices were characterized using Oriel IQE 200.

DFT Calculation

The DFT calculations were carried out with the Vienna ab initio Simulation Package (VASP). The electro-ion interactions were described by the projector-augmented wave (PAW) pseudopotentials. The generalized gradient approximation (GGA) was used with the Perdew-Burke-Ernzerhof (PBE) exchange-correlation functional. A cutoff energy of 500 eV was used for the plane-wave basis set. In all calculations, the

convergence criterion for minimum energy and minimum force during geometrical optimization was used as 10^{-6} eV and 0.01 eV/Å, respectively. A $Cs_{0.125}MA_{0.125}FA_{0.75}Pb(I_{0.833}Br_{0.167})_3$ composition was achieved by replacing two FA^+ molecules with one MA^+ molecule and Cs atom as well as four I atoms with Br atoms of a 2 × 2 × 2 supercell of the tetragonal unit cell of $FAPbI_3$. Two types of (001) surface slab models with PbI_2 and I atoms as terminal as well as a vacuum layer of 20 Å thickness were constructed based on the $Cs_{0.125}MA_{0.125}FA_{0.75}Pb(I_{0.833}Br_{0.167})_3$ supercell. A k-point sampling of 2 × 2 × 1 was used for structural optimizations. We used the VASPKIT code for postprocessing of the VASP calculated data. The adsorption energy was calculated as: $E(slab*PEA^+) – E(slab) – E(PEA^+)$, where the three terms denote the total energies of slab with PEA^+, slab without PEA^+ and PEA^+.

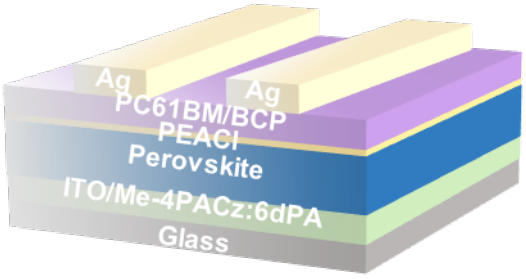

Figure S1. Schematic illustration of the PIN device structure of WB-PSCs.

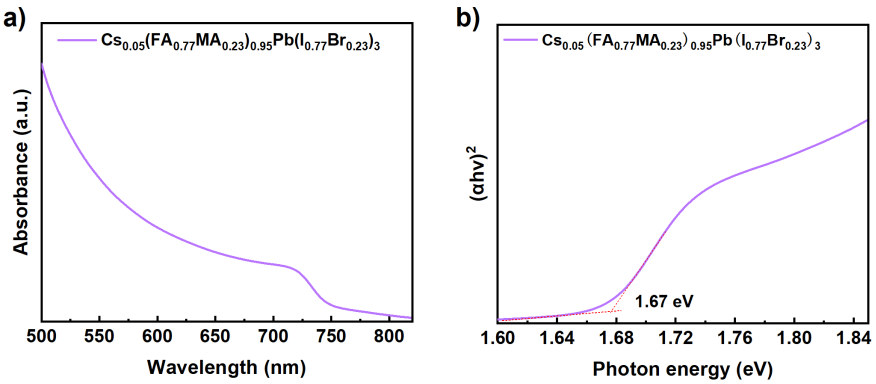

Figure S2. a) The absorption spectrum and b) Tauc plot of the perovskite film.

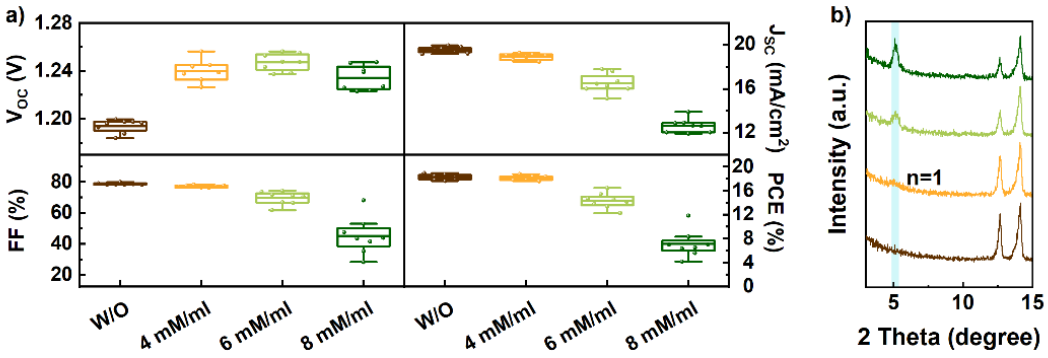

Figure S3. a) Statistical distribution of the photovoltaic parameters of the WB-PSCs treated with PEACl at different concentrations. b) XRD patterns of the wide bandgap perovskite films treated with PEACl at different concentrations. After the PEACl treatment, there was no subsequent annealing process (PEACl_No Ann).

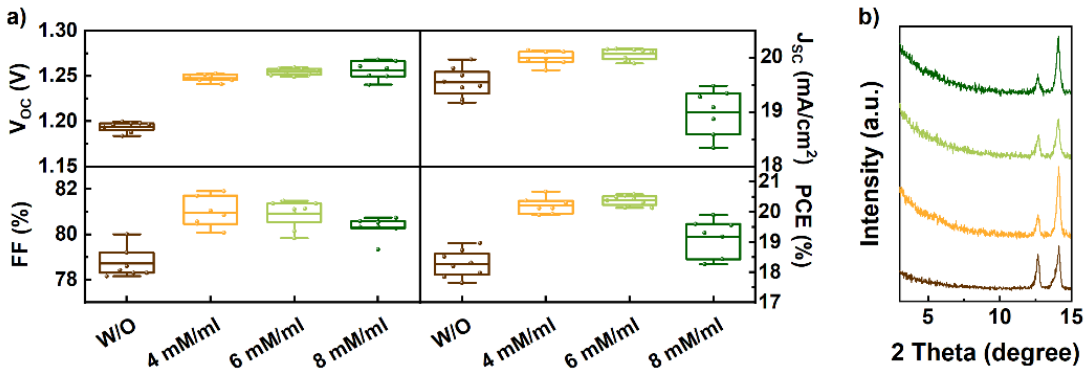

Figure S4. a) Statistical distribution of photovoltaic parameters of the WB-PSCs treated with PEACl at different concentrations. b) XRD patterns of the wide bandgap perovskite films treated with PEACl at different concentrations. After the PEACl treatment, these perovskite films were further annealed at 100 ℃ for 10 minutes (PEACl_Ann).

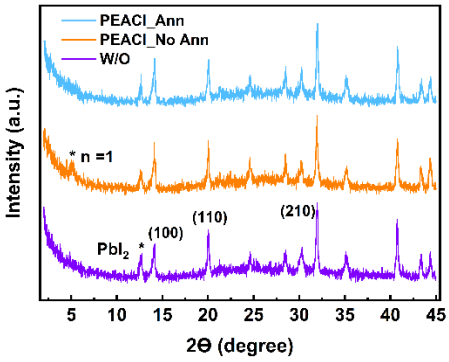

Figure S5. XRD patterns of the wide bandgap perovskite films treated with PEACl without annealing or with annealing.

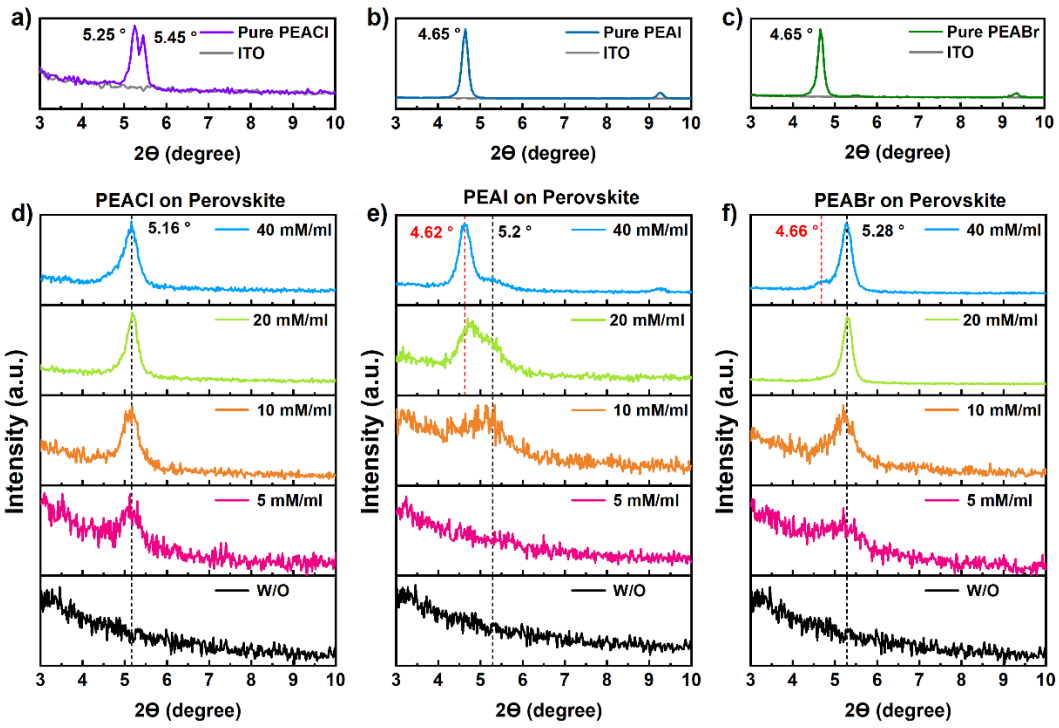

Figure S6. XRD patterns of pure a) PEACl, b) PEAI, and c) PEABr (0.05 °/step). XRD patterns of PEAX (X = Cl, I, and Br) with different concentrations (5, 10, 20, 40 mM/ml) on perovskite films: d) PEACl, e) PEAI, and f) PEABr (0.02 °/step). The XRD pattern of ITO in Figure S6(a-c) is the same data plot.

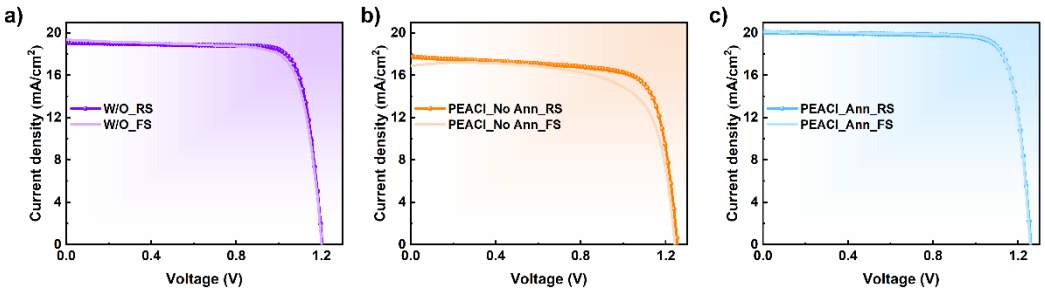

Figure S7. Current density versus voltage (*J-V*) characteristics of the WB-PSCs a) W/O, b) PEACl_No Ann, and c) PEACl_Ann.

Table S1. The photovoltaic parameters extracted from the forward or reverse scan from *J-V* curves of the WB-PSCs.

	V_{OC} (V)	J_{SC} (mA/cm^2)	FF (%)	PCE (%)
W/O_RS	1.20	19.08	80.99	18.61
W/O_FS	1.20	19.39	77.38	18.03
PEACl_No Ann_RS	1.25	17.76	75.28	16.77
PEACl_No Ann_FS	1.24	16.91	71.15	14.95
PEACl_Ann_RS	1.26	20.05	81.57	20.61
PEACl_Ann_FS	1.26	20.09	81.68	20.62

Table S2. Summary of photovoltaic performance of the state-of-the-art PIN wide-bandgap perovskite solar cells from 2020 to 2023.

Bandgap (eV)	V_{OC} deficit (mV)	V_{OC} (V)	J_{SC} (mA/cm^2)	FF (%)	PCE (%)	Ref.
1.79	530	1.26	16.94	80.17	17.04	[2]
1.79	530	1.26	17.9	78.9	17.8	[3]
1.79	540	1.25	16.9	83	17.6	[4]
1.78	590	1.19	18.53	80.3	17.71	[5]
1.77	480	1.29	15	77.9	15.1	[6]
1.77	486	1.284	17.2	80.29	17.72	[7]
1.75	430	1.32	18.7	82.2	20.3	[8]
1.73	418	1.312	18.89	81.6	20.22	[9]
1.73	480	1.25	19.48	78.9	19.07	[10]
1.72	530	1.19	18.7	78.4	17.4	[11]
1.72	370	1.35	17.2	81.20	18.90	[12]
1.71	520	1.19	19.6	79.00	18.30	[13]
1.69	480	1.21	20.7	80.50	20.10	[14]
1.68	510	1.17	21.27	80.48	20.02	[15]
1.68	400	1.28	-	-	21.5	[16]
1.68	470	1.21	20.98	79.45	20.11	[17]
1.68	430	1.25	20.32	81.35	20.66	[18]
1.68	460	1.22	22.1	76	20.5	[19]
1.68	490	1.19	20.94	81.80	20.31	[20]
1.67	485	1.185	20.9	80.7	20	[21]
1.67	410	1.26	20.05	81.57	20.61	This work
1.66	430	1.23	20.79	82.28	21.05	[22]
1.65	400	1.25	21.1	83	21.9	[23]
1.65	430	1.22	21.5	83.3	21.9	[24]

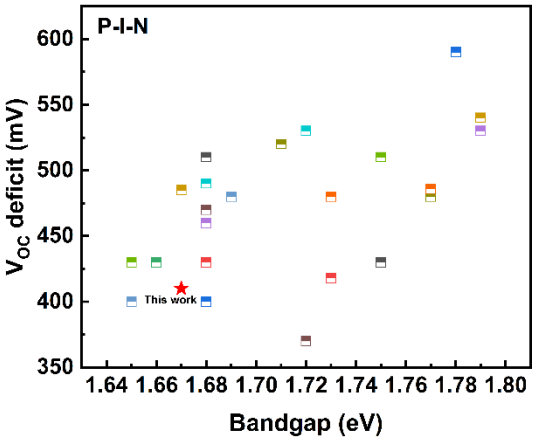

Figure S8. Graphical representation of V_{OC} deficit of the state-of-the-art PIN wide-bandgap perovskite solar cells from 2020 to 2023 presented in Table S2.

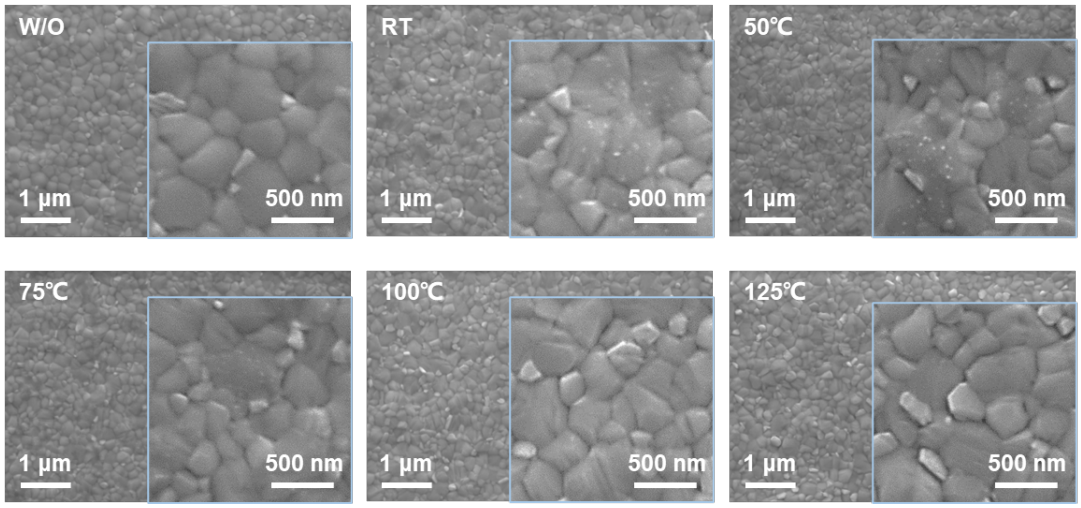

Figure S9. SEM images of the perovskite films with PEACl at different annealing temperatures for 10 minutes.

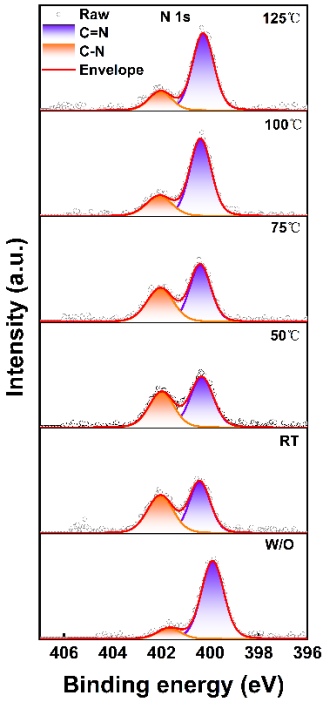

Figure S10. XPS N 1s spectra of the perovskite films with PEACl at different annealing temperatures for 10 minutes.

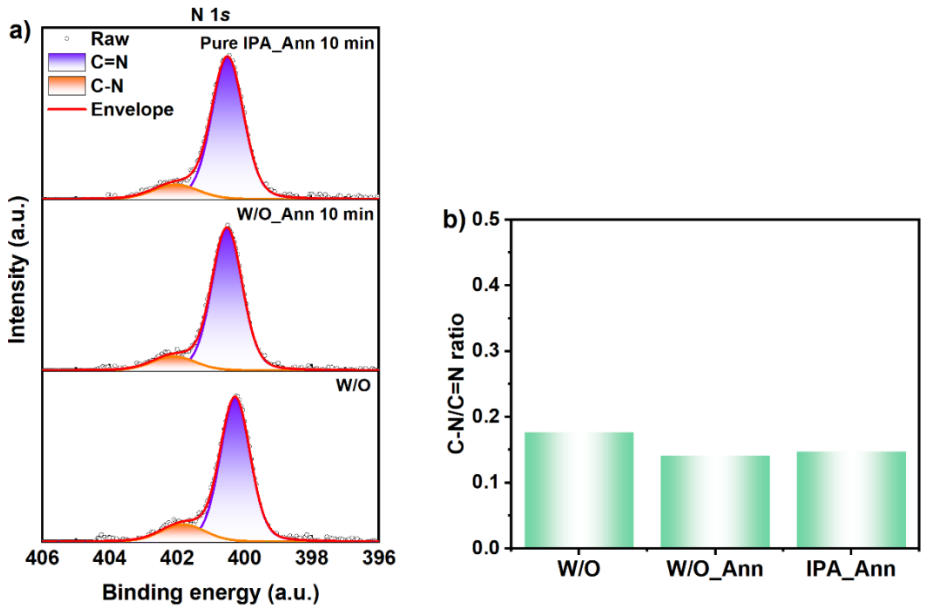

Figure S11. a) XPS N 1*s* spectra of the perovskite films with different treatments. b) Intensity ratios of C-N to C=N binding extracted from the XPS N 1*s* spectra.

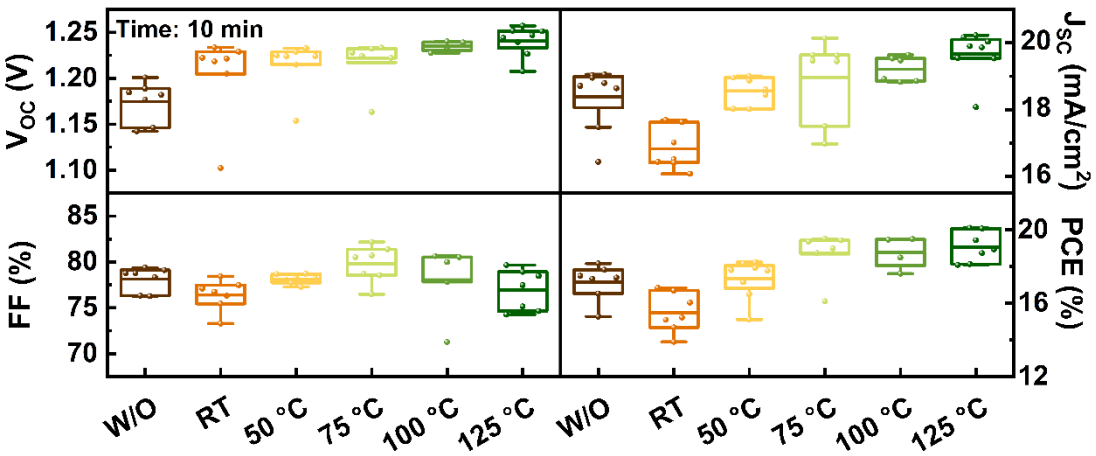

Figure S12. Statistical distribution of the photovoltaic parameters of the WB-PSCs treated with PEACl annealing at different temperatures for 10 minutes.

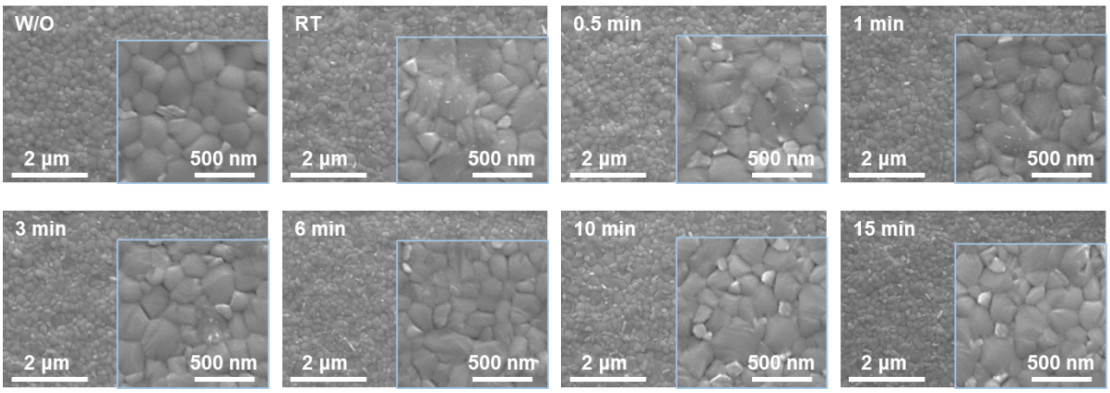

Figure S13. SEM images of the perovskite films with PEACl annealing at 100 ℃ for different time.

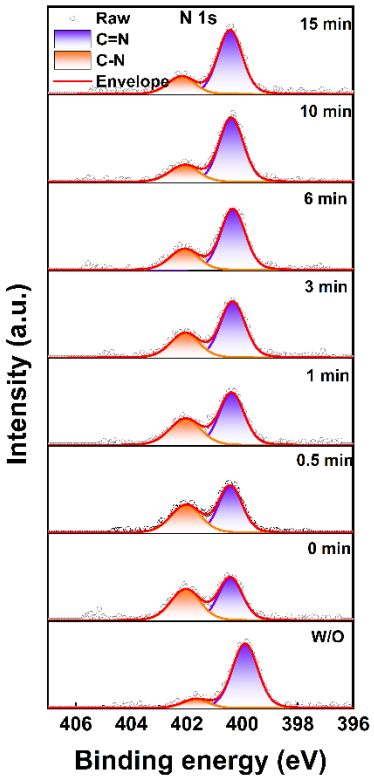

Figure S14. XPS N 1s spectra of the perovskite films with PEACl annealing at 100 ℃ for different times.

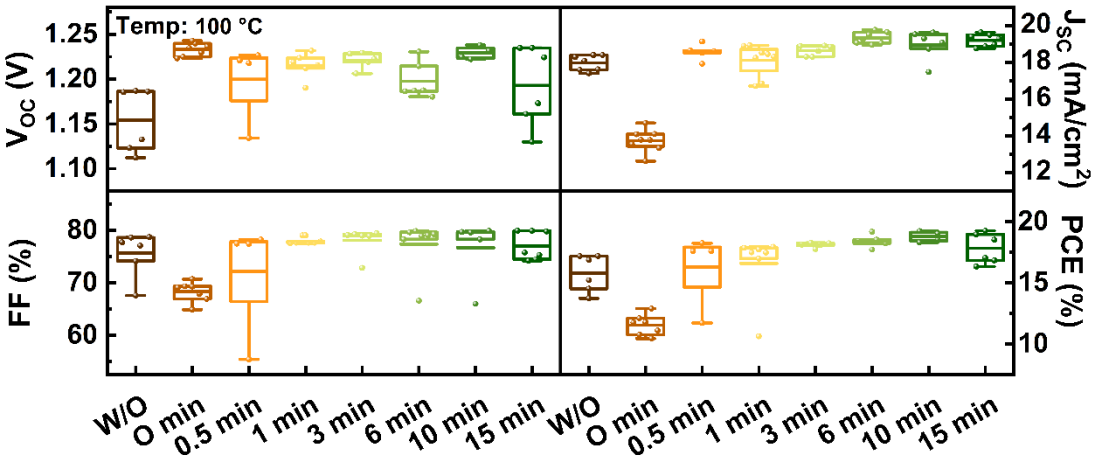

Figure S15. Statistical distribution of the photovoltaic parameters of WB-PSCs treated with PEACl annealing at 100 ℃ for different times.

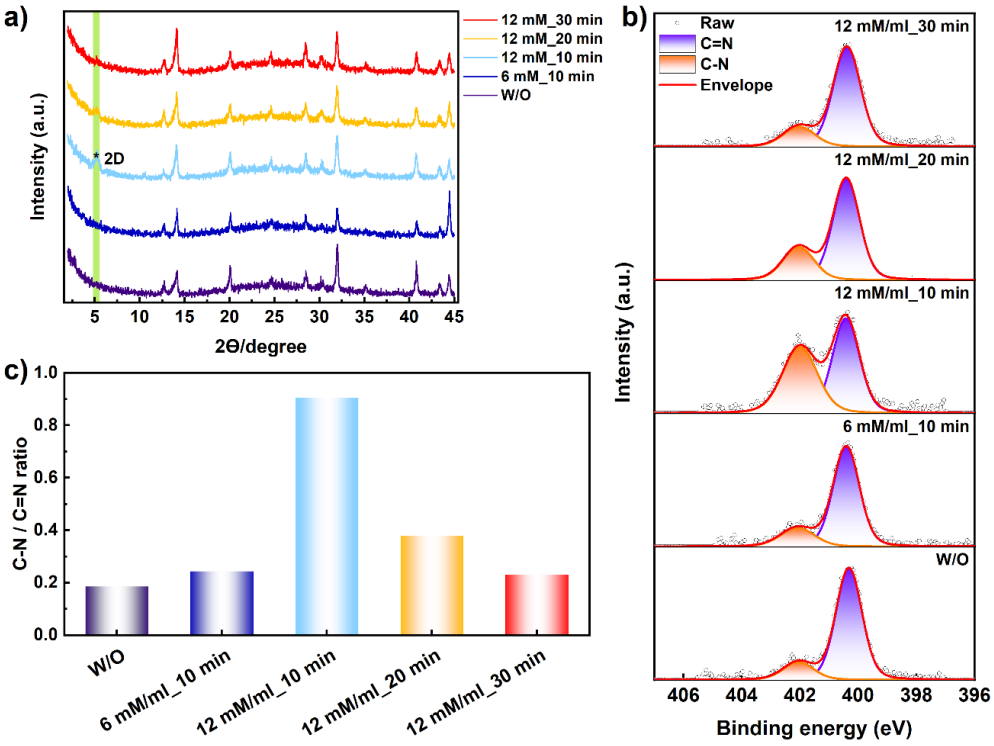

Figure S16. a) XRD patterns, b) XPS N 1*s* spectra, and c) intensity ratios of C-N to C=N binding extracted from the XPS N 1*s* spectra of the perovskite films treated with PEACl with different concentrations and times.

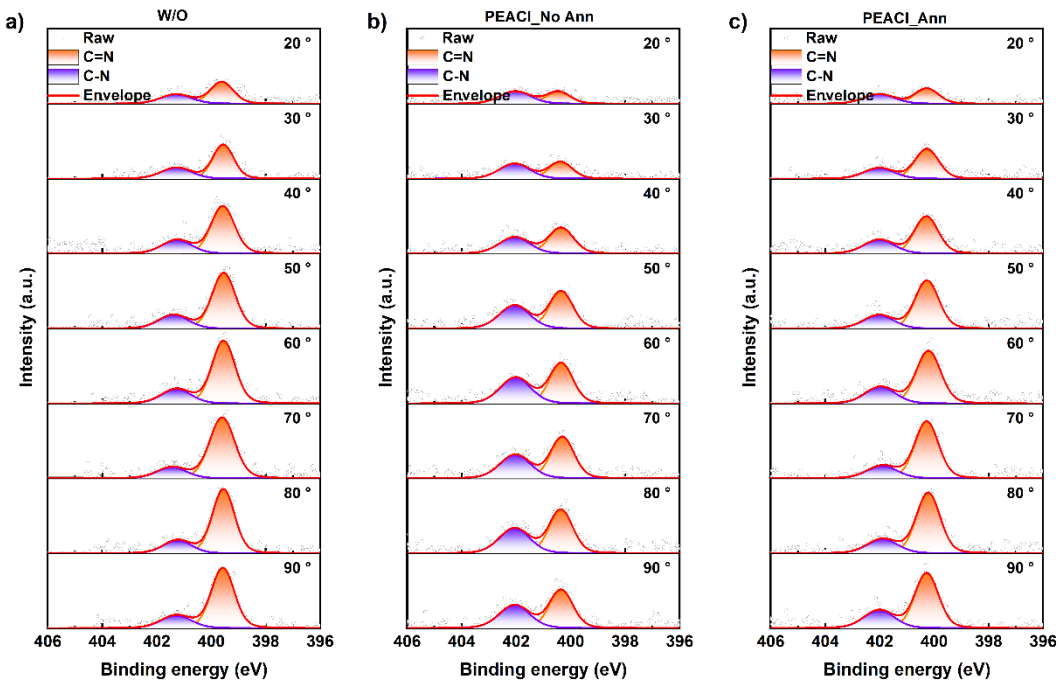

Figure S17. Angle-dependent XPS spectra of the N 1s region of a) W/O, b) PEACl_No Ann, and c) PEACl_Ann perovskite films.

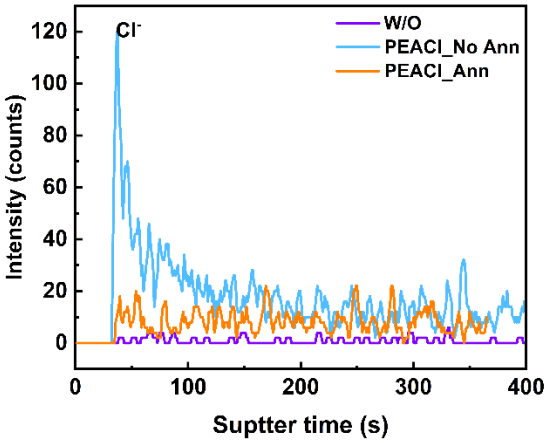

Figure S18. The distribution of Cl^- in perovskite films obtained from SIMS profiles.

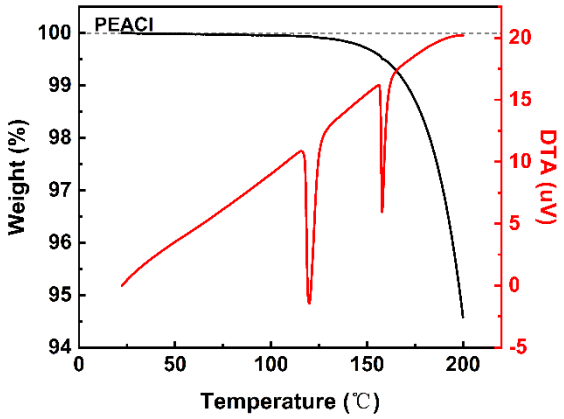

Figure S19. The TGA/DTA analyses of the fresh PEACl powder.

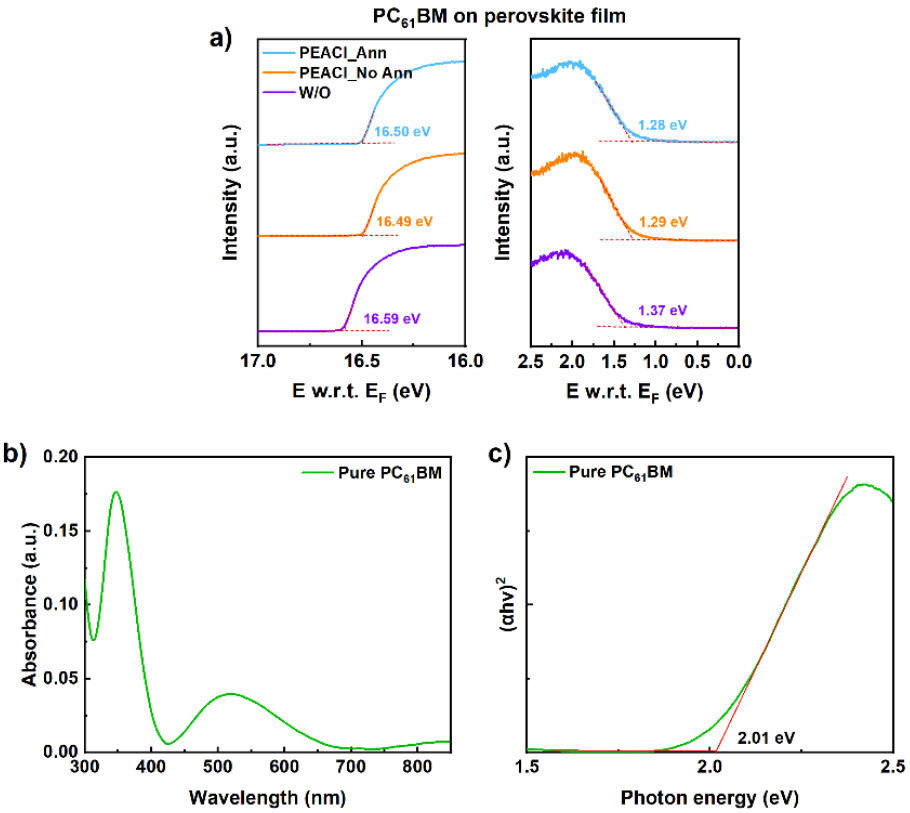

Figure S20. a) UPS results of $PC_{61}BM$. $PC_{61}BM$ was spin-coated on the perovskite films with different treatments. b) The absorption spectra and c) Tauc plots of pure $PC_{61}BM$.

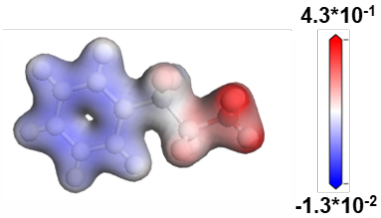

Figure S21. Electrostatic potential of PEA^+.

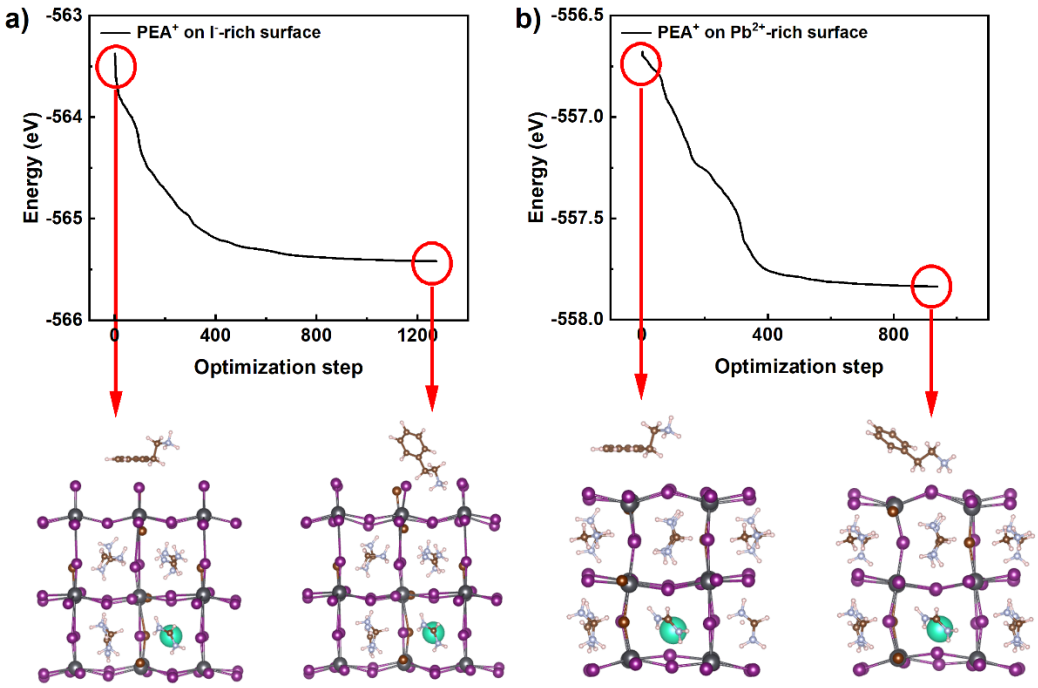

Figure S22. The energy change over the optimization time of the PEA^+ on the a) I^--rich surface and b) Pb^{2+}-rich surface.

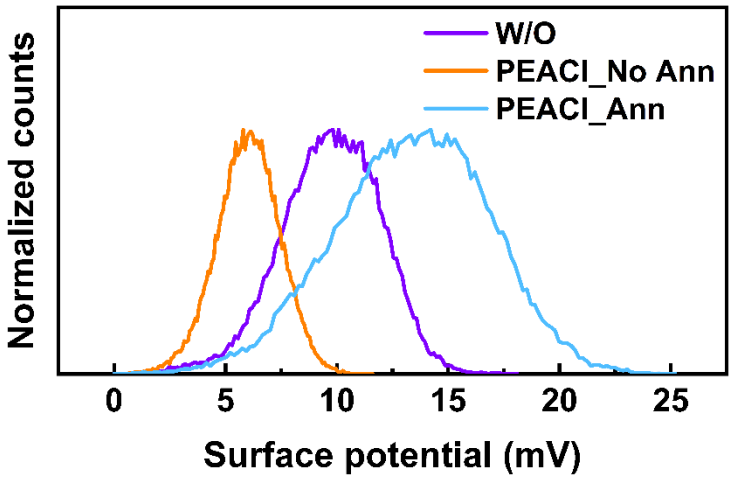

Figure S23. Statistical CPD distribution of the perovskite films from KPFM results in Fig. 4(e)-(g).

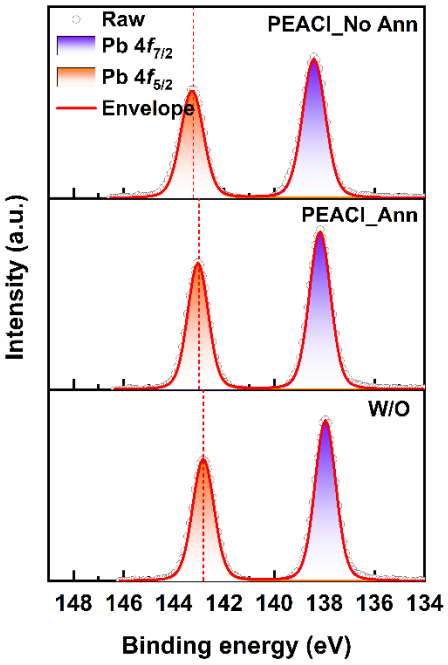

Figure S24. XPS Pb 4*f* region of the three types of perovskite films.

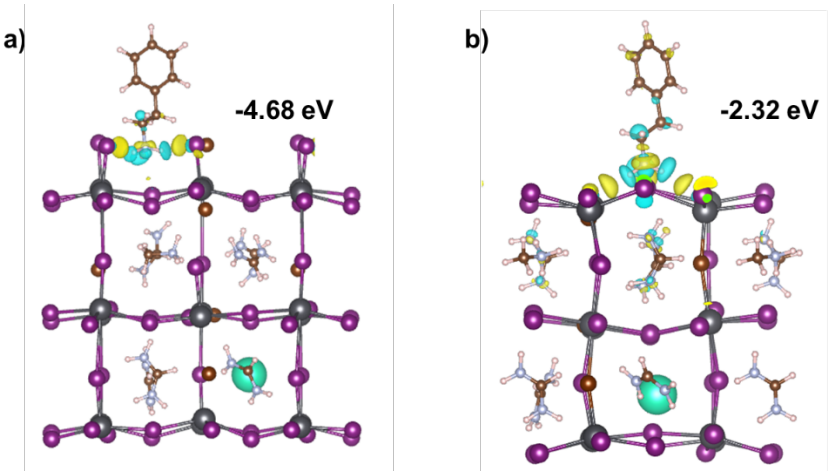

Figure S25. Electron density differences for the PEA^{+} molecule on a) I^{-} -rich and b) Pb^{2+} -rich surfaces of the perovskite, and the resulting binding energies.

Table S3. The energy of the PEA^+ molecule.

Molecule	Energy (eV)
PEA^+	-122.20

Table S4. The energies of the I^--rich and Pb^{2+}-rich surface.

Surface	E_{slab} (eV) [a]	E_{ads} (eV) [b]	E_{BE} (eV) [c]
I^--rich surface	-438.62	-565.50	-4.68
Pb^{2+}-rich surface	-433.74	-558.26	-2.32

[a] E_{slab} is the energy of the optimized slab model of the surface. [b] E_{ads} is the energy of the optimized model of the surface with PEA^+. [c] E_{BE} is the binding energy of the surface and the PEA^+.

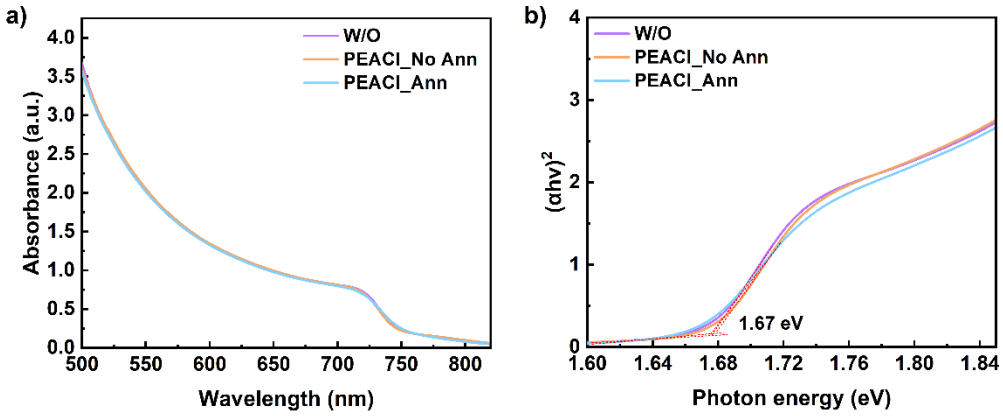

Figure S26. a) The absorption spectra and b) Tauc plots of the perovskite films.

Table S5. TRPL fitting data of the perovskite films.

ETL	Films	τ_1 (ns)	A_1	τ_2 (ns)	A_2
With ETL	W/O	1.8	468269	6.9	2533
	PEACl_No Ann	3.2	34328	11.7	1487
	PEACl_Ann	1.9	329412	5.9	2827
Without ETL	W/O	7.1	1630	23.2	1269
	PEACl_No Ann	30.9	1935	88.5	521
	PEACl_Ann	25.2	1353	140.9	1203

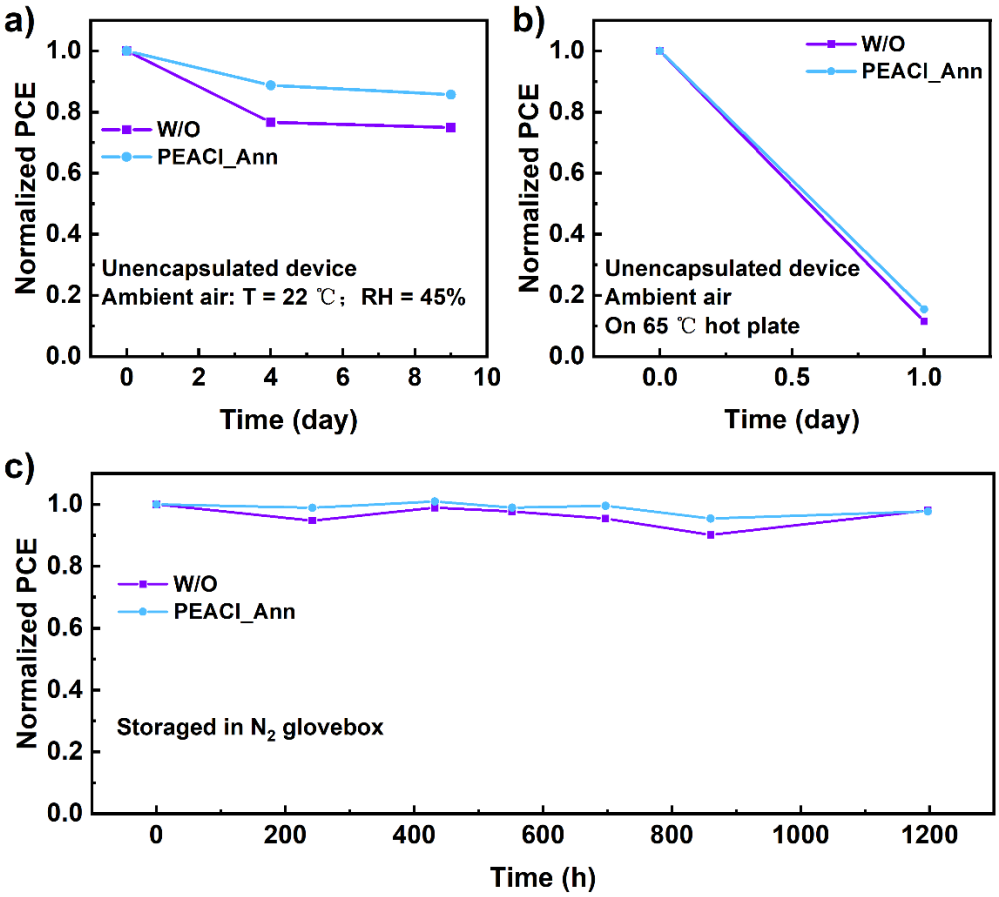

Figure S27. a) Stability of unencapsulated devices exposed to ambient air in the dark (ISOS-D-1). b) Stability of unencapsulated devices exposed to ambient air in the dark and heated on a hot plate at 65 °C (ISOS-D-2). c) Long-term storage stability of the devices performed in the dark inside a N_2 glovebox (ISOS-D-1I).

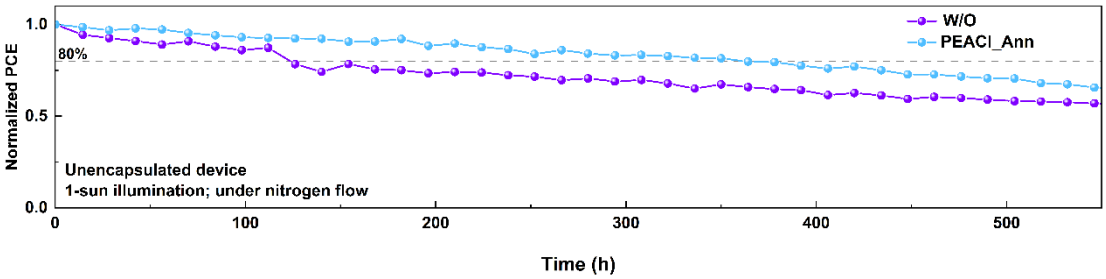

Figure S28. Long-term operational stability of unencapsulated devices at room temperature under nitrogen flow and measured at a fixed bias.

Table S6. Summary of stability of the PIN WB-PSCs treated with ammonium ligands.

Perovskite	Bandgap (eV)	Strategy	PCE (%)	Stability	Ref.
$Cs_{0.05}(FA_{0.77}MA_{0.23})_{0.95}Pb(I_{0.77}Br_{0.23})_3$	1.67	Control (W/O)	18.61	T_{80} = 130 h (RT)	This work
		PEACl_Ann	20.61	T_{80} = 380 h (RT)	
$(FA_{0.65}MA_{0.2}Cs_{0.15})Pb(I_{0.8}Br_{0.2})_3$	1.68	PEAI	17.46	T_{80} = 200 h (RT)	[25]
		$PEA(I_{0.25}SCN_{0.75})$	20.7	T_{80} = 1000 h (RT)	
		PEASCN	18.83	T_{80} < 50 h (RT)	
$Cs_{0.2}FA_{0.8}Pb(I_{0.6}Br_{0.4})_3$	1.78	PEAI	19.6	T_{90} = 1040 h (RT)	[26]
$Cs_{0.05}MA_{0.05}FA_{0.9}Pb(I_{0.95}Br_{0.05})_3$	/	PEAI	20.1	T_{80} ~ 220 h (85 ℃)	[27]
		345FAnI	20.2	T_{80} ~ 810 h(85 ℃)	
$FA_{0.8}Cs_{0.2}Pb(I_{0.7}Br_{0.3})_3$	1.75	GABr	18.19	T_{80} > 100 h (RT)	[28]
$(FA_{0.65}MA_{0.20}Cs_{0.15})Pb(I_{0.8}Br_{0.2})_3$	1.68	PEAI + $Pb(SCN)_2$	18.9	<4% degradation stored over 4000 h	[29]
$FA_{0.8}Cs_{0.15}MA_{0.05}Pb(I_{0.82}Br_{0.18})_3$	1.65	PEAI+MASCN	21.9	Maintained initial PCE after 500 h (LED light source)	[24]
$FA_{0.8}Cs_{0.2}Pb(I_{0.6}Br_{0.4})_3$	1.77	Control	16.06	T_{75} = 21 h (RT)	[30]
		PEABr	17.74	T_{90} = 103 h (RT)	

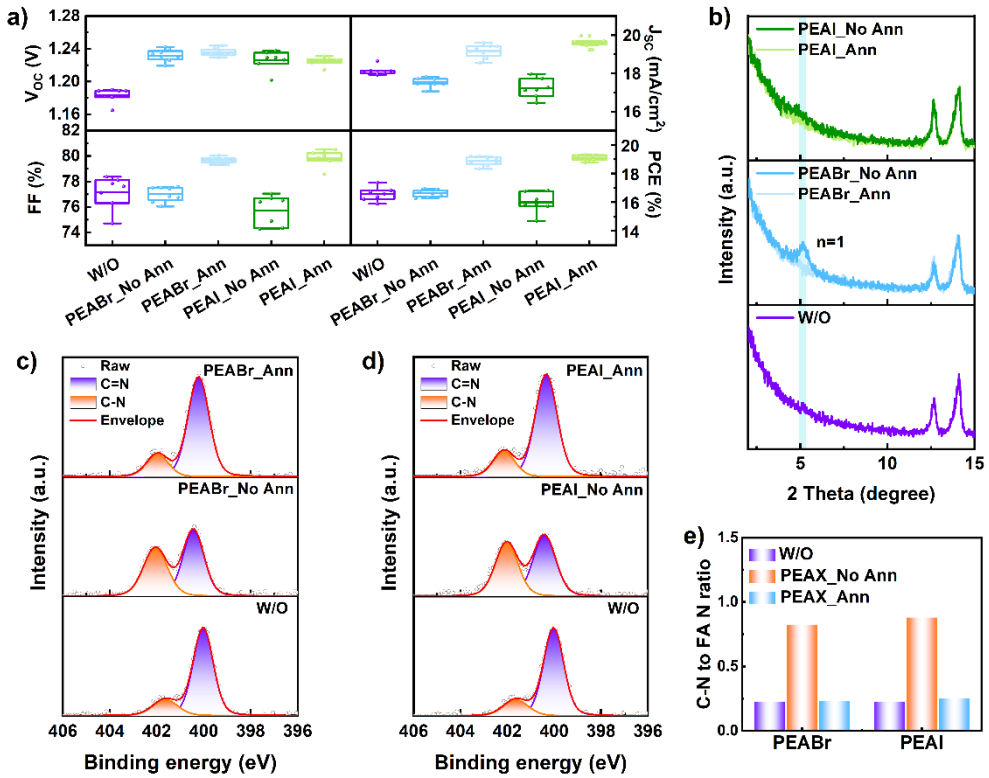

Figure S29. a) Statistical distribution of the photovoltaic parameters of the WB-PSCs and b) XRD patterns of the perovskite films treated with PEAX annealing and no annealing. XPS N 1s region of the perovskite films treated with c) PEABr and d) PEAI. e) XPS N 1s region C-N to FA N ratio of the perovskite films treated with PEAX annealing and no annealing.

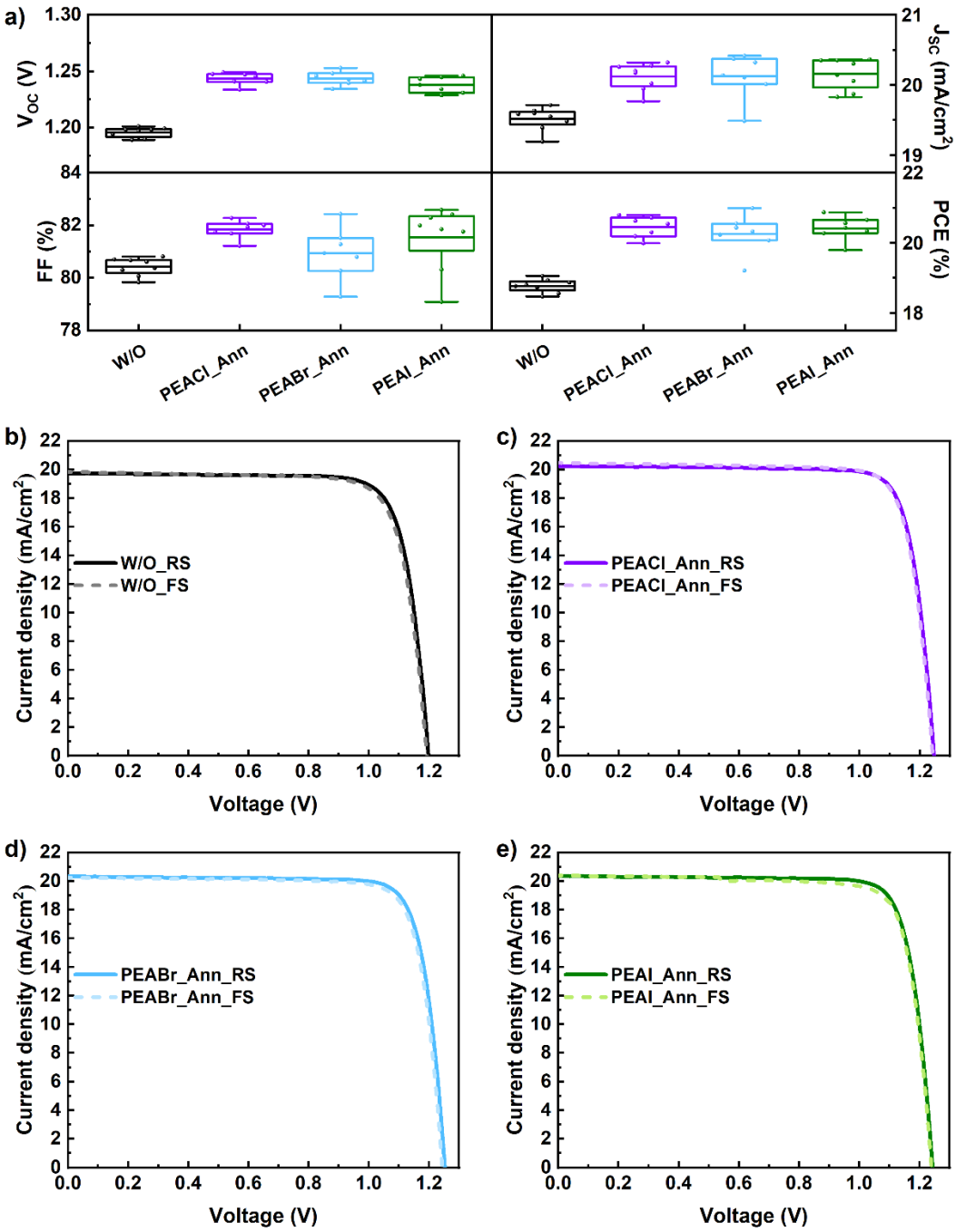

Figure S30. a) Statistical distribution of photovoltaic parameters of PIN structured WB-PSCs treated with PEACl, PEABr, and PEAI in a single batch of experiment. The *J-V* characteristics from the forward or reverse scans of the WB-PSCs b) W/O, c) PEACl_Ann, d) PEABr_Ann, and e) PEAI_Ann.

Table S7. The champion photovoltaic parameters extracted from the forward and reverse scans of the *J-V* curves of the WB-PSCs.

Devices	V_{OC} (V)	J_{SC} (mA/cm^2)	FF (%)	PCE (%)
W/O-RS	1.20	19.71	80.67	19.05
W/O-FS	1.19	19.86	79.12	18.74
PEACl_Ann_RS	1.25	20.26	82.28	20.79
PEACl_Ann_FS	1.24	20.48	81.45	20.73
PEABr_Ann_RS	1.25	20.32	82.42	20.99
PEABr_Ann_FS	1.24	20.26	81.78	20.61
PEAI_Ann_RS	1.24	20.37	82.41	20.87
PEAI_Ann_FS	1.24	20.40	80.94	20.47

Supplementary Note 1

Discussion about the n = 1 2D phase formation on the perovskite films.

Since PEABr and PEAI will also be used later in this paper, in this supplementary text, we analyze the XRD patterns of all three PEAX. It should be noted that, for this experiment, the PEAX layers are all not annealed.

To further confirm that the XRD pattern at 5.16° 2θ shown in **Figure S5** is the n = 1 2D phase and not the excess PEAX, we measured the XRD patterns of the pure PEAX on glass/ITO. The pure PEACl shows two characteristic patterns, at 5.25° and 5.45° 2θ, respectively (**Figure S6a**). PEAI and PEABr show the same pattern, which is at 4.65° 2θ (**Figure S6b, c**). Then, we increased the concentrations of PEAX and spin-coated PEAX on the perovskite films to get a clearer 2D pattern on the perovskite films. As shown in **Figure S6d**, the perovskite films treated with PEACl show the XRD pattern at 5.16° 2θ, which is different from that of the pure PEACl (5.25° and 5.45° 2θ), suggesting that the XRD pattern at 5.16° 2θ shown in **Figure S5** is n = 1 2D phase and not the pure PEACl. For PEAI spin-coated on the perovskite films (**Figure S6e**), there is almost only one pattern at around 5.2° 2θ when the concentration of PEAI is lower than 20 mM/ml, then when the concentration of PEAI is increased, another pattern at around 4.62° 2θ appears (red dotted line), which is corresponding to the pure PEAI (4.65° 2θ), considering the intervals error. Similarly, for PEABr spin-coated on the perovskite films (**Figure S6f**), the n = 1 2D phase appears at 5.28° 2θ when the concentration of PEABr is lower than 40 mM/ml, and the pattern of excess PEABr appears at 4.66° 2θ (red dotted line) when the concentration reaches 40 mM/ml.

Therefore, when the perovskite film is treated with a relatively low concentration of PEAX (as for device fabrication, 4 mM/ml) and without annealing, the n = 1 2D phase can be formed, and excess PEAX is only detected when the concentration is very high.

Supplementary Note 2

The results of $Cs_{0.2}FA_{0.8}Pb(I_{0.8}Br_{0.2})_3$ and $MAPbI_3$ perovskite devices and films treated with PEACl without and with annealing.

1) $Cs_{0.2}FA_{0.8}Pb(I_{0.8}Br_{0.2})_3$

First, the PIN-structured PSCs were fabricated using the following device architecture: ITO/Me-4PACz:6dPA/$Cs_{0.2}FA_{0.8}Pb(I_{0.8}Br_{0.2})_3$/PEACl/$PC_{61}BM$/BCP/Ag. PEACl is used as a type of post-treatment on the $Cs_{0.2}FA_{0.8}Pb(I_{0.8}Br_{0.2})_3$ perovskite, which bandgap is determined from the ultraviolet-visible (UV-Vis) spectrum and the corresponding Tauc Plot (Fig. S31(a)-(b)) being 1.67 eV. The statistical distribution of photovoltaic (PV) parameters of the PSCs is shown with the box chart graphs in Fig. S32(a), and the champion PV parameters are summarized in Table S8. X-ray diffraction (XRD) patterns are shown in Fig. S32(b)-(c). These results show that the $Cs_{0.2}FA_{0.8}Pb(I_{0.8}Br_{0.2})_3$ perovskite devices treated with PEACl show a similar behavior to the wide bandgap perovskite ($Cs_{0.05}(FA_{0.77}MA_{0.23})_{0.95}Pb(I_{0.77}Br_{0.23})_3$) used in our original manuscript. PEACl_No Ann treated $Cs_{0.2}FA_{0.8}Pb(I_{0.8}Br_{0.2})_3$ devices show a much lower power conversion efficiency (PCE) (14.68% on average) than the W/O devices (17.72% on average), and the film treated with PEACl_No Ann also shows a 2D phase at approximately 5.16° from the XRD patterns. On the other hand, the PEACl_Ann devices without the 2D phase, show an enhanced device performance (18.77% on average).

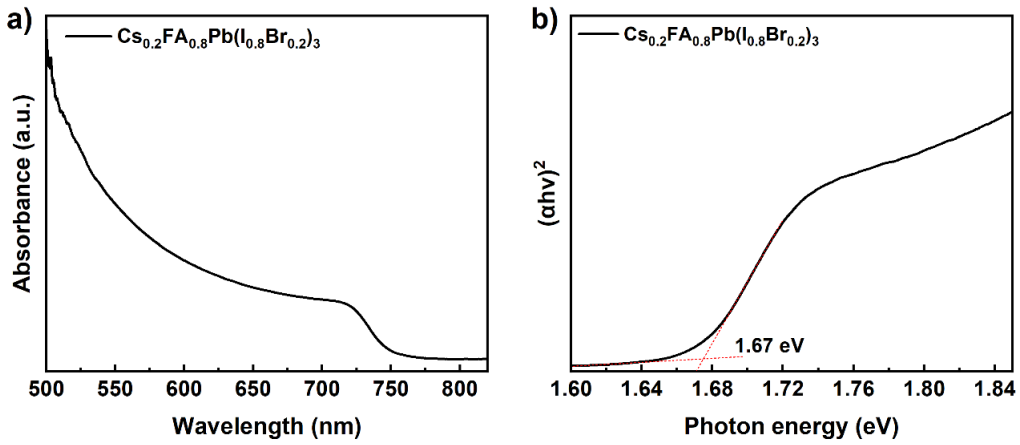

Figure S31. a) The absorption spectrum and b) Tauc plot of the $Cs_{0.2}FA_{0.8}Pb(I_{0.8}Br_{0.2})_3$ film.

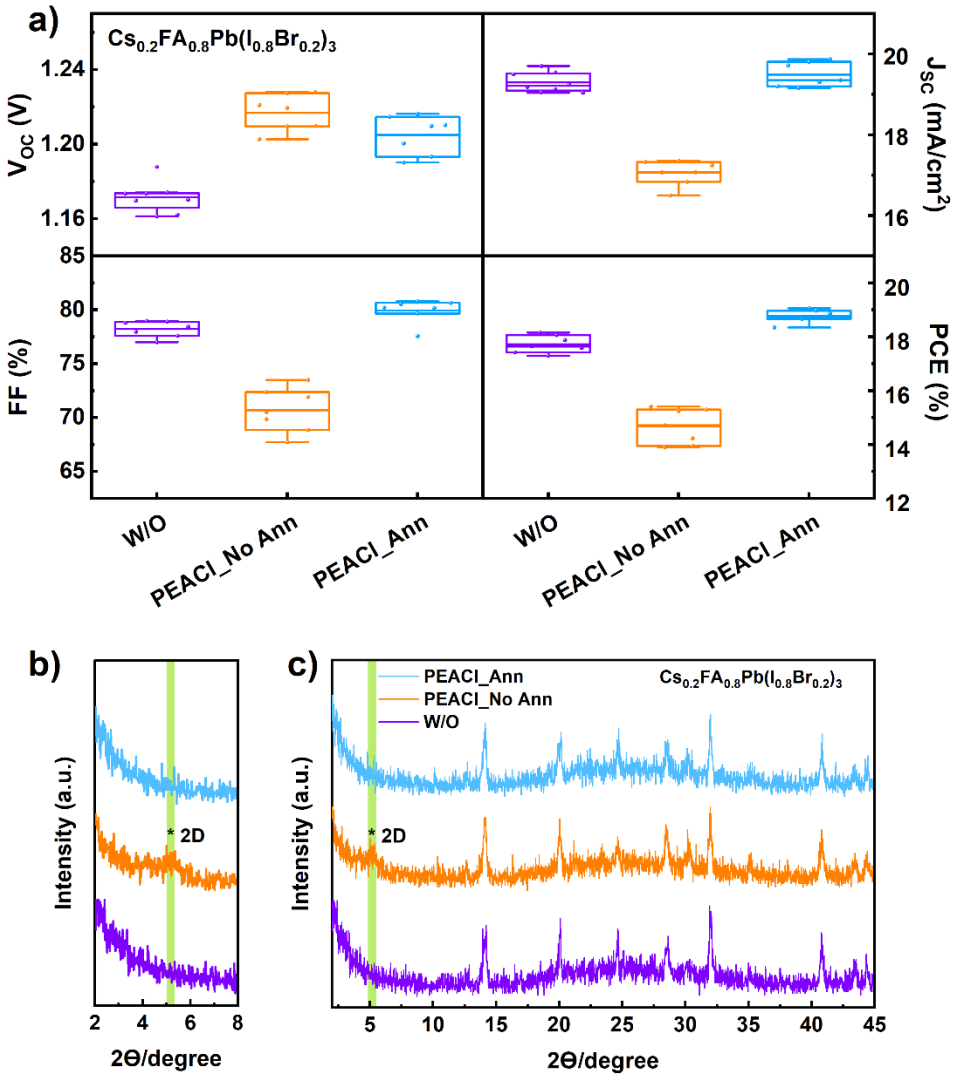

Figure S32. a) Statistical distribution of the photovoltaic parameters of the PIN-structured $Cs_{0.2}FA_{0.8}Pb(I_{0.8}Br_{0.2})_3$ PSCs. XRD patterns of the $Cs_{0.2}FA_{0.8}Pb(I_{0.8}Br_{0.2})_3$ films treated with PEACl without and with annealing: b) 2θ from 2° to 8°, c) 2θ from 2° to 45°.The 2D phase appears at 2θ around 5.16°(green line).

Table S8. The champion photovoltaic parameters extracted from *J-V* curves of the $Cs_{0.2}FA_{0.8}Pb(I_{0.8}Br_{0.2})_3$ PSCs.

Devices	V_{OC} (V)	J_{SC} (mA/cm^2)	FF (%)	PCE (%)
W/O	1.17	19.70	78.80	18.16

PEACl_No Ann	1.23	17.07	73.50	15.41
PEACl_Ann	1.22	19.30	80.79	18.97

Furthermore, the XPS N 1*s* spectra were employed to determine the PEACl content on the $Cs_{0.2}FA_{0.8}Pb(I_{0.8}Br_{0.2})_3$ perovskite surface. As shown in Fig. S33(a)-(b), there is only one main peak for the $Cs_{0.2}FA_{0.8}Pb(I_{0.8}Br_{0.2})_3$ perovskite film without the PEACl treatment, which is the C=N signal originating from formamidinium (FA^+).[31-34] When the film is treated with PEACl_No Ann, the other non-negligible peak appears at around 402 eV, which represents the C-N bond deriving from adding PEA^+ on the perovskite surface, indicating the presence of PEA^+ on the perovskite surface and the formation of the 2D phase. However, after PEACl is annealed, the signal of the C-N bond is reduced significantly and becomes almost negligible.

These results indicate that this phenomenon is also applicable for MA^+-free perovskite ($Cs_{0.2}FA_{0.8}Pb(I_{0.8}Br_{0.2})_3$) case, i.e., the PEACl surface treatment without annealing produces the n = 1 2D phase, which decreases the device performance. On the other hand, if the PEACl is annealed, the PCE increases as the 2D phase disappears.

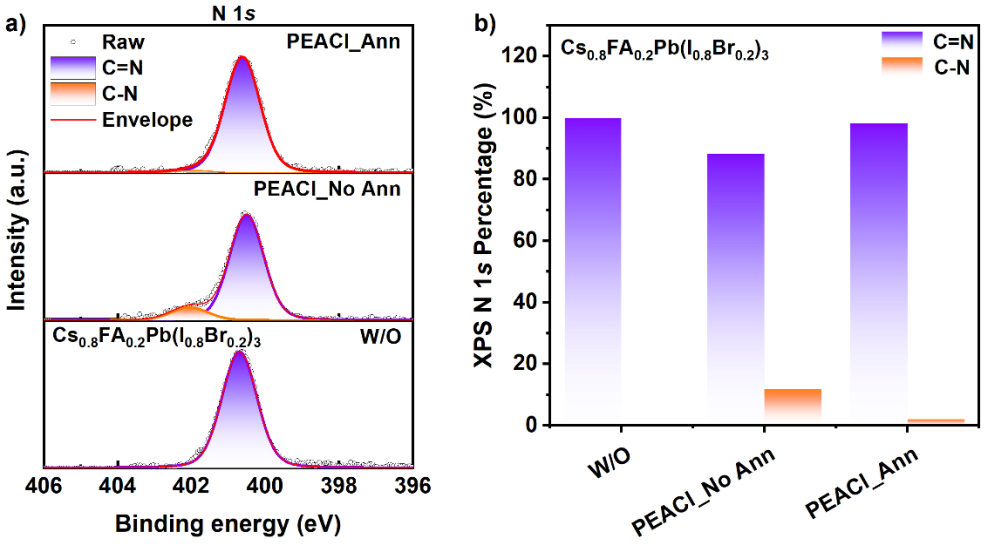

Figure S33. a) XPS N 1*s* spectra of the $Cs_{0.2}FA_{0.8}Pb(I_{0.8}Br_{0.2})_3$ perovskite films treated with PEACl without and with annealing. b) Summary of XPS N 1*s* percentage from Figure S@(a).

2) $MAPbI_3$

Similarly, the PIN-structured $MAPbI_3$ PSCs were fabricated using the following device architecture: ITO/Me-4PACz:6dPA/$MAPbI_3$/PEACl/$PC_{61}BM$/BCP/Ag. The statistical distribution of the PV parameters of the PSCs is shown with the box chart graphs in Fig. S34(a), and the champion PV parameters are summarized in Table S9. XRD patterns are shown in Fig. S34(b). The results show that the $MAPbI_3$ perovskite devices treated with PEACl_No Ann and PEACl_Ann show similar results to the wide bandgap perovskite used in this work. The PEACl_No Ann treated $MAPbI_3$ devices show a significantly lower PCE (7.8% on average) than the W/O devices (18.54% on average), and the film treated with PEACl_No Ann also shows a 2D phase at 2θ around 5.16° based on the XRD patterns. On the other hand, the PEACl_Ann devices, without the 2D phase, show an enhanced device performance (18.88% on average).

The XPS N 1*s* spectra of the $MAPbI_3$ perovskite films are shown in Fig. S34(c), however due to the presence of only C-N bond signal it is hard to notice significant differences of the PEACl amount. Therefore, XPS C 1*s* spectra were employed to provide further information about the PEACl influence on the perovskite surface. As shown in Fig. S34(d)-(e), for the pure $MAPbI_3$ sample without PEACl treatment, the C-N peak is dominant, but when the $MAPbI_3$ is treated with PEACl_No Ann, the intensity of C-C is much stronger than C-N peak, which comes mainly from the C-C bonds of PEA^+. In addition, the C-C bond ratio decreases after PEACl is annealed, which is consistent with the 2D phase disappearance. It is found that the ratio of the C-C signal is still higher than the C-N signal in the PEACl_Ann sample, indicating the presence of PEA^+ left on the $MAPbI_3$ film even if the 2D phase is decomposed, which is also consistent with the conclusion observed for the wide bandgap perovskite.

Therefore, this behavior is also observed in the case of to $MAPbI_3$ PSCs.

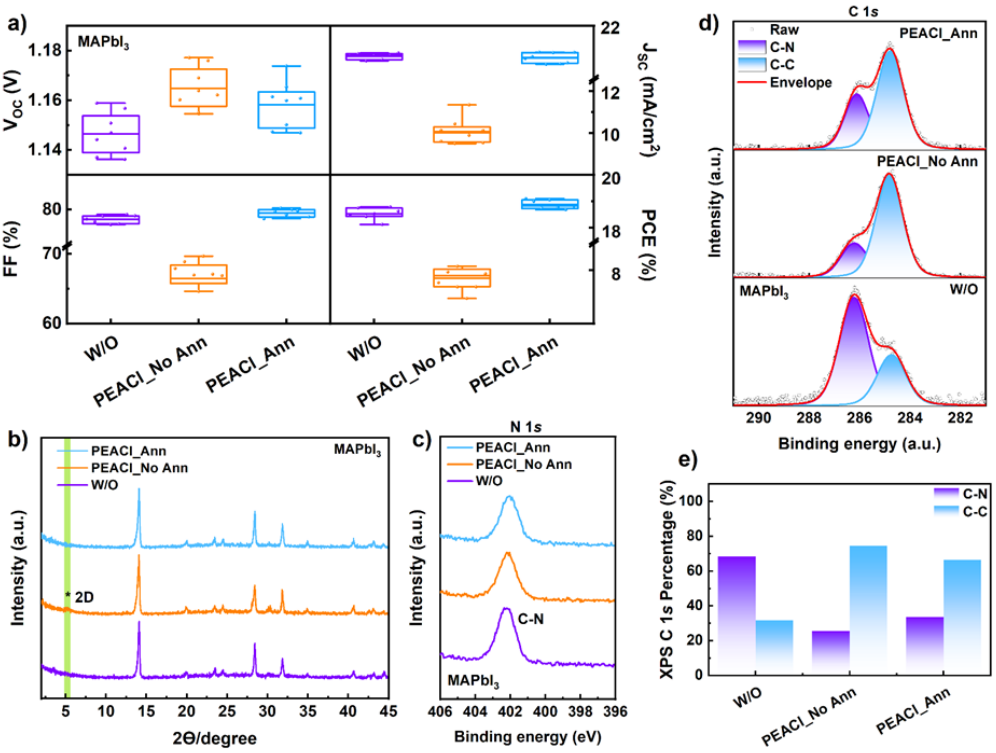

Figure S34. a) Statistical distribution of the photovoltaic parameters of the PIN-structured $MAPbI_3$ PSCs. b) XRD patterns of the $MAPbI_3$ films treated with PEACl without and with annealing. c) XPS N 1*s* spectra and d) XPS C 1*s* spectra of the $MAPbI_3$ perovskite films treated with PEACl without and with annealing. e) Summary of XPS C 1*s* percentage from Figure S34(d).

Table S9. The champion photovoltaic parameters extracted from *J-V* curves of the $MAPbI_3$ PSCs.

Devices	V_{OC} (V)	J_{SC} (mA/cm^2)	FF (%)	PCE (%)
W/O	1.15	20.59	79.28	18.79
PEACl_No Ann	1.16	11.34	69.68	9.20
PEACl_Ann	1.16	20.53	80.20	19.10

In summary, for the PIN-structured PSCs, the PEA^+-induced n = 1 2D phase formed on the perovskite surface would lead to a decreased device performance, and the n = 1 2D phase is eliminated after the PEAX is treated with the subsequent annealing process as the PEA^+ is volatilized. We have demonstrated that the PEA^+(halide) treated PIN-structured PSCs can also be applied to the MA^+-free and pure $MAPbI_3$ perovskites, which provides the initial hints that the

method may be considered as a universal phenomenon. However, due to the numerous varieties of possible perovskite compositions, we would like to limit the discussion on the relatively small number of perovskite materials that have been examined in our study.

References

[1] Z. Liu, L. Qiu, E. J. Juarez-Perez, Z. Hawash, T. Kim, Y. Jiang, Z. Wu, S. R. Raga, L. K. Ono, S. Liu, Y. B. Qi, *Nature Communications* **2018**, 9, 3880.

[2] C. Wang, W. Shao, J. Liang, C. Chen, X. Hu, H. Cui, C. Liu, G. Fang, C. Tao, *Small* **2022**, 18, e2204081.

[3] W. Chen, Y. Zhu, J. Xiu, G. Chen, H. Liang, S. Liu, H. Xue, E. Birgersson, J. W. Ho, X. Qin, J. Lin, R. Ma, T. Liu, Y. He, A. M.-C. Ng, X. Guo, Z. He, H. Yan, A. B. Djurišić, Y. Hou, *Nature Energy* **2022**, 7, 229.

[4] S. Qin, C. Lu, Z. Jia, Y. Wang, S. Li, W. Lai, P. Shi, R. Wang, C. Zhu, J. Du, J. Zhang, L. Meng, Y. Li, *Advanced Materials* **2022**, 34, 2108829.

[5] K. M. Reza, A. Gurung, B. Bahrami, A. H. Chowdhury, N. Ghimire, R. Pathak, S. I. Rahman, M. A. R. Laskar, K. Chen, R. S. Bobba, B. S. Lamsal, L. K. Biswas, Y. Zhou, B. Logue, Q. Qiao, *Solar RRL* **2021**, 5, 2000740.

[6] H. Lai, J. Luo, Y. Zwirner, S. Olthof, A. Wieczorek, F. Ye, Q. Jeangros, X. Yin, F. Akhundova, T. Ma, R. He, R. K. Kothandaraman, X. Chin, E. Gilshtein, A. Müller, C. Wang, J. Thiesbrummel, S. Siol, J. M. Prieto, T. Unold, M. Stolterfoht, C. Chen, A. N. Tiwari, D. Zhao, F. Fu, *Advanced Energy Materials* **2022**, 12, 2202438.

[7] R. He, Z. Yi, Y. Luo, J. Luo, Q. Wei, H. Lai, H. Huang, B. Zou, G. Cui, W. Wang, C. Xiao, S. Ren, C. Chen, C. Wang, G. Xing, F. Fu, D. Zhao, *Advanced Science* **2022**, 9, e2203210.

[8] Q. Jiang, J. Tong, R. A. Scheidt, X. Wang, A. E. Louks, Y. Xian, R. Tirawat, A. F. Palmstrom, M. P. Hautzinger, S. P. Harvey, S. Johnston, L. T. Schelhas, B. W. Larson, E. L. Warren, M. C. Beard, J. J. Berry, Y. Yan, K. Zhu, *Science* **2022**, 378, 1295.

[9] Y. Zhao, C. Wang, T. Ma, L. Zhou, Z. Wu, H. Wang, C. Chen, Z. Yu, W. Sun, A. Wang, H. Huang, B. Zou, D. Zhao, X. Li, *Energy & Environmental Science* **2023**, 16, 2080.

[10] C. Chen, Z. Song, C. Xiao, R. A. Awni, C. Yao, N. Shrestha, C. Li, S. S. Bista, Y. Zhang, L. Chen, R. J. Ellingson, C.-S. Jiang, M. Al-Jassim, G. Fang, Y. Yan, *ACS Energy Letters* **2020**, 5, 2560.

[11] Y.-M. Xie, Q. Yao, Z. Zeng, Q. Xue, T. Niu, R. Xia, Y. Cheng, F. Lin, S.-W. Tsang, A. K. Y. Jen, H.-L. Yip, Y. Cao, *Advanced Functional Materials* **2022**, 32, 2112126.

[12] Z. Liu, J. Siekmann, B. Klingebiel, U. Rau, T. Kirchartz, *Advanced Energy Materials* **2021**, 11, 2003386.

[13] J. Liang, C. Chen, X. Hu, Z. Chen, X. Zheng, J. Li, H. Wang, F. Ye, M. Xiao, Z. Lu, Y. Xu, S. Zhang, R. Yu, C. Tao, G. Fang, *ACS Applied Materials & Interfaces* **2020**, 12, 48458.

[14] F. Peña-Camargo, P. Caprioglio, F. Zu, E. Gutierrez-Partida, C. M. Wolff, K. Brinkmann, S. Albrecht, T. Riedl, N. Koch, D. Neher, M. Stolterfoht, *ACS Energy Letters* **2020**, 5, 2728.

[15] G. Cui, X. Zhang, Y. Zhu, C. Chen, Z. Gao, J. Wang, G. Xie, H. Huang, B. Zou, D. Zhao, *Journal of Materials Chemistry C* **2023**, 11, 10259.

[16] S. Mariotti, E. Köhnen, F. Scheler, K. Sveinbjörnsson, L. Zimmermann, M. Piot, F. Yang, B. Li, J. Warby, A. Musiienko, D. Menzel, F. Lang, S. Keßler, I. Levine, D. Mantione, A. Al-Ashouri, M. S. Härtel, K. Xu, A. Cruz, J. Kurpiers, P. Wagner, H. Köbler, J. Li, A. Magomedov, D. Mecerreyes, E. Unger, A. Abate, M. Stolterfoht, B. Stannowski, R. Schlatmann, L. Korte, S. Albrecht, *Science* **2023**, 381, 63.

[17] Y. Zheng, X. Wu, J. Liang, Z. Zhang, J. Jiang, J. Wang, Y. Huang, C. Tian, L. Wang, Z. Chen, C.-C. Chen, *Advanced Functional Materials* **2022**, 32, 2200431.

[18] J. Chen, D. Wang, S. Chen, H. Hu, Y. Li, Y. Huang, Z. Zhang, Z. Jiang, J. Xu, X. Sun, S. K. So, Y. Peng, X. Wang, X. Zhu, B. Xu, *ACS Applied Materials & Interfaces* **2022**, 14, 43246.

[19] F. H. Isikgor, F. Furlan, J. Liu, E. Ugur, M. K. Eswaran, A. S. Subbiah, E. Yengel, M. De Bastiani, G. T. Harrison, S. Zhumagali, C. T. Howells, E. Aydin, M. Wang, N. Gasparini, T. G. Allen, A. u. Rehman, E. Van Kerschaver, D. Baran, I. McCulloch, T. D. Anthopoulos, U. Schwingenschlögl, F. Laquai, S. De Wolf, *Joule* **2021**, 5, 1566.

[20] C. Chen, J. Liang, J. Zhang, X. Liu, X. Yin, H. Cui, H. Wang, C. Wang, Z. Li, J. Gong, Q. Lin, W. Ke, C. Tao, B. Da, Z. Ding, X. Xiao, G. Fang, *Nano Energy* **2021**, 90, 106608.

[21] J. Liang, C. Chen, X. Hu, M. Xiao, C. Wang, F. Yao, J. Li, H. Wang, J. He, B. Da, Z. Ding, W. Ke, C. Tao, G. Fang, *Solar RRL* **2021**, 5, 2100249.

[22] D. Wang, H. Guo, X. Wu, X. Deng, F. Li, Z. Li, F. Lin, Z. Zhu, Y. Zhang, B. Xu, A. K. Y. Jen, *Advanced Functional Materials* **2022**, 32, 2107359.

[23] G. Yang, Z. Ni, Z. J. Yu, B. W. Larson, Z. Yu, B. Chen, A. Alasfour, X. Xiao, J. M. Luther, Z. C. Holman, J. Huang, *Nature Photonics* **2022**, 16, 588.

[24] Z. Liu, C. Zhu, H. Luo, W. Kong, X. Luo, J. Wu, C. Ding, Y. Chen, Y. Wang, J. Wen, Y. Gao, H. Tan, *Advanced Energy Materials* **2023**, 13, 2203230.

[25] D. Kim, H. J. Jung, I. J. Park, B. W. Larson, S. P. Dunfield, C. Xiao, J. Kim, J. Tong, P. Boonmongkolras, S. G. Ji, F. Zhang, S. R. Pae, M. Kim, S. B. Kang, V. Dravid, J. J. Berry, J. Y. Kim, K. Zhu, D. H. Kim, B. Shin, *Science* **2020**, 368, 155.

[26] J. Wen, Y. Zhao, P. Wu, Y. Liu, X. Zheng, R. Lin, S. Wan, K. Li, H. Luo, Y. Tian, L. Li, H. Tan, *Nature Communications* **2023**, 14, 7118.

[27] S. M. Park, M. Wei, J. Xu, H. R. Atapattu, F. T. Eickemeyer, K. Darabi, L. Grater, Y. Yang, C. Liu, S. Teale, B. Chen, H. Chen, T. Wang, L. Zeng, A. Maxwell, Z. Wang, K. R. Rao, Z. Cai, S. M. Zakeeruddin, J. T. Pham, C. M. Risko, A. Amassian, M. G. Kanatzidis, K. R. Graham, M. Grätzel, E. H. Sargent, *Science* **2023**, 381, 209.

[28] C. Chen, Z. Song, C. Xiao, D. Zhao, N. Shrestha, C. Li, G. Yang, F. Yao, X. Zheng, R. J. Ellingson, C.-S. Jiang, M. Al-Jassim, K. Zhu, G. Fang, Y. Yan, *Nano Energy* **2019**, 61, 141.

[29] D. H. Kim, C. P. Muzzillo, J. Tong, A. F. Palmstrom, B. W. Larson, C. Choi, S. P. Harvey, S. Glynn, J. B. Whitaker, F. Zhang, Z. Li, H. Lu, M. F. A. M. van Hest, J. J. Berry, L. M. Mansfield, Y. Huang, Y. Yan, K. Zhu, *Joule* **2019**, 3, 1734.

[30] R. He, Z. Yi, Y. Luo, J. Luo, Q. Wei, H. Lai, H. Huang, B. Zou, G. Cui, W. Wang, C. Xiao, S. Ren, C. Chen, C. Wang, G. Xing, F. Fu, D. Zhao, *Advanced Science* **2022**, 9, 2203210.

[31] Q. Yao, Q. Xue, Z. Li, K. Zhang, T. Zhang, N. Li, S. Yang, C. J. Brabec, H.-L. Yip, Y. Cao, *Advanced Materials* **2020**, 32, 2000571.

[32] L. Li, Y. Lv, Q. Liu, Z. Fan, R. Yuan, W. Tang, X. Liu, P. Zhang, W.-H. Zhang, *Journal of Materials Chemistry A* **2022**, 10, 9161.

[33] S. Béchu, M. Ralaiarisoa, A. Etcheberry, P. Schulz, *Advanced Energy Materials* **2020**, 10, 1904007.

[34] T. Bu, L. K. Ono, J. Li, J. Su, G. Tong, W. Zhang, Y. Liu, J. Zhang, J. Chang, S. Kazaoui, F. Huang, Y.-B. Cheng, Y. B. Qi, *Nature Energy* **2022**, 7, 528.